

Contents lists available at ScienceDirect

Petroleum Science

journal homepage: www.keaipublishing.com/en/journals/petroleum-science



Original Paper

A fast amplitude preserving three-parameter 3D parabolic Radon transform and its application on multiple attenuation



Ii-Tao Ma ^{a, b, c, *}, Kai-Ge Zhao ^{a, b, c}, Zhen Liao ^{a, b, c}

- ^a College of Geophysics, China University of Petroleum (Beijing), Beijing, 102249, China
- b State Key Laboratory of Petroleum Resources and Engineering, China University of Petroleum (Beijing), Beijing, 102249, China
- ^c CNPC Key Laboratory of Geophysical Prospecting, China University of Petroleum (Beijing), Beijing, 102249, China

ARTICLE INFO

Article history: Received 28 March 2024 Received in revised form 4 June 2024 Accepted 17 June 2024 Available online 18 June 2024

Edited by Meng-Jiao Zhou

Keywords: Three-parameter 3D Radon Orthogonal polynomial Amplitude-preserving Multiple attenuation

ABSTRACT

Seismic wavefields propagate through three-dimensional (3D) space, and their precise characterization is crucial for understanding subsurface structures. Traditional 2D algorithms, due to their limitations, are insufficient to fully represent three-dimensional wavefields. The classic 3D Radon transform algorithm assumes that the wavefield's propagation characteristics are consistent in all directions, which often does not hold true in complex underground media. To address this issue, we present an improved 3D threeparameter Radon algorithm that considers the wavefield variation with azimuth and provides a more accurate wavefield description. However, introducing new parameters to describe the azimuthal variation also poses computational challenges. The new Radon transform operator involves five variables and cannot be simply decomposed into small matrices for efficient computation; instead, it requires large matrix multiplication and inversion operations, significantly increasing the computational load. To overcome this challenge, we have integrated the curvature and frequency parameters, simplifying all frequency operators to the same, thereby significantly improving computation efficiency. Furthermore, existing transform algorithms neglect the lateral variation of seismic amplitudes, leading to discrepancies between the estimated multiples and those in the data. To enhance the amplitude preservation of the algorithm, we employ orthogonal polynomial fitting to capture the amplitude spatial variation in 3D seismic data. Combining these improvements, we propose a fast, amplitude-preserving, 3D threeparameter Radon transform algorithm. This algorithm not only enhances computational efficiency while maintaining the original wavefield characteristics, but also improves the representation of seismic data by increasing amplitude fidelity. We validated the algorithm in multiple attenuation using both synthetic and real seismic data. The results demonstrate that the new algorithm significantly improves both accuracy and computational efficiency, providing an effective tool for analyzing seismic wavefields in complex subsurface structures.

© 2024 The Authors. Publishing services by Elsevier B.V. on behalf of KeAi Communications Co. Ltd. This is an open access article under the CC BY-NC-ND license (http://creativecommons.org/licenses/by-nc-nd/4.0/).

1. Introduction

The Radon transform is a widely used mathematical transform in medical CT image reconstruction and seismic data processing. It has proven to be effective in identifying seismic events, attenuating multiples, reconstructing seismic data, analyzing velocities, and separating wavefields. In the field of seismic data processing, Radon transform can be categorized into linear, parabolic, and hyperbolic transforms.

* Corresponding author. E-mail address: majitao@cup.edu.cn (J.-T. Ma). Radon transform was originally proposed by the Austrian mathematician Radon in 1917. In the 1970s, the geophysical group at Stanford University began focusing the research on Radon transform, leading to significant progress and important contributions to its application in seismic data processing. Hampson (1986) further improved the linear Radon to parabolic and applied it to multiple attenuation. The parabolic Radon transform utilizes the velocity differences between primaries and multiples to suppress multiples. After normal moveout correction, the primaries are flattened, while the multiples are partially corrected from hyperbolas to parabolas, which can be described by parabolic curves. By mapping these parabolas in the time space domain into points in

Radon domain using parabolic Radon transform, the multiples and primaries with different curvatures can be separated in the transformed domain, and multiple attenuation can be achieved by muting.

Beylkin (1987) discussed Radon transform based on the least-squares (LS) theory. The resolution of LS algorithm result is relatively low, and there are many methods available for improving the Radon domain resolution. There are large-scale time domain inversion algorithms (Thorson and Claerbout, 1985; Stoffa et al., 1981; Yilmaz and Taner, 1994), iterative reweighting frequency domain algorithms (Sacchi and Ulrych, 1995; Cary, 1998; Herrmann et al., 2000; Chen and Lu, 2011), and hybrid time-frequency methods (Lu, 2013; Wang et al., 2019; Li and Li, 2017), but they are beyond the scopes discussed in our article. The proposed method in the paper mainly focuses on the 3D extension and amplitude preserving of the Radon algorithms.

The propagation of seismic waves is three-dimensional, and simple 2D Radon transforms cannot depict them accurately. Given the complexity of subsurface media and the characteristics of seismic wave propagation in 3D space, it is necessary to develop 3D Radon algorithms. 3D Radon sums up seismic data along predefined 3D paraboloids, and it can simultaneously consider seismic data in the inline and crossline directions, resulting in more accurate mapping of events in 3D space. In complex areas where 2D algorithms may not fully capture the characteristics of seismic data, 3D algorithms are more adaptable. Based on 3D algorithms, the propagation paths of multiples can be completely characterized, leading to improved multiple suppression results. Moreover, 3D algorithms offer higher data resolution by considering more spatial information. A 3D seismic gather composed of bin gathers from different azimuths can be constructed. And using bin gathers is more intuitive to describe the three-dimensional wave propagation. Consequently, the 3D Radon algorithm can be applied to seismic data in small bin gathers. A 3D common-cell gather can also be assembled according to the value of scaler offsets. Due to the time difference at different azimuths, the assembled data is jittered along the offset direction.

The research of 3D Radon transform begins with linear Radon transform and the scholars mainly study its application in interpolation and denoising. For example, Donati and Martin (1995) firstly used 3D linear Radon transform in seismic data interpolation and reconstruction. Zhang and Lu (2014) proposed an accelerated 3D sparse time-invariant linear Radon transform in the mixed time-frequency domain based on iterative threshold shrinkage algorithm, and applied it in the interpolation and reconstruction of 3D pre-stack seismic data. Cao and Ross (2017) proposed a high-resolution 3D linear Radon transform based on matching pursuit, which effectively dealt with the spatial aliasing, improved the resolution and achieved a good interpolation effect. Sun et al. (2022) proposed a 3D conical linear Radon transform for random noise, multiple and surface wave suppression in 3D seismic gathers. There is hardly no research on 3D parabolic Radon transforms before 2008.

Existing 3D Radon transform represents the 3D seismic wavefield using two parameters, which are q_x and q_y , with q_x the parameter depicting the wavefield in inline direction, and q_y the parameter depicting the wavefield in crossline direction. The 3D algorithm requires that the shape of seismic events in each bin gather is consistent, in which case the time slice of seismic data is a standard ellipse with the focal points located on the survey line. However, when anisotropy exists underground, the shape of seismic events will change, and the ellipse of the time slice will also rotate, which makes the existing 3D Radon algorithm unable to accurately describe 3D seismic data.

Hugonnet et al. (2008, 2009) considered the azimuthal effects

by incorporating an elliptical model for the variations of the seismic events with azimuth, and proposed a high-resolution 3D parabolic Radon transform based on lower frequencies constraints. Ma (2024) referred the description of ellipse in mathematics, introduced an extra parameter q_{xy} to describe the rotation ellipse of time slice, and proposed a 3D parabolic Radon algorithm based on the rotated ellipse model, which is also called three-parameter (q_x , q_y , and q_{xy}) 3D Radon transform in this paper. The algorithm accounts for anisotropy and is capable of accurately characterizing seismic data that varies with azimuth. Ma (2022) also proposed a high resolution three-parameter 3D Radon transform based on lower frequencies constraints, and achieved very good multiple attenuation result on synthetic data. But the computation cost of the high-resolution method is huge.

Unlike traditional algorithms, the three-parameter 3D Radon transform cannot decompose the whole Radon operator into operators in inline and crossline directions separately, and can only multiply and invert very large matrices for each frequency, which leads to low computation efficiency. Abbad et al. (2011) proposed a modified fast algorithm for 2D parabolic Radon transform. In this fast algorithm, the curvature and frequency are combined into a new parameter, denoted as λ . The transform operator is independent of frequency, thus simplifying the algorithm to a single operator problem. This necessitates the transform operator inversion only once, with the inverted result being subsequently called for all frequency computations, significantly enhancing computational efficiency. Li et al. (2013) and Sun et al. (2019) both studied the fast Radon transform from the aspects of resolution enhancement and amplitude preserving, respectively. Wang et al. (2017) studied the amplitude preserved seismic data reconstruction by twoparameter fast 3D parabolic Radon transform. They all introduced new variables $\lambda_x = q_x f$ and $\lambda_y = q_y f$, so that it only needs to calculate the inverse of the transform operator once during the data reconstruction, saving a large amount of computational time. Xie et al. (2021) proposed a multiple-suppression method using the twoparameter fast high-resolution parabolic Radon transform with curvature magnification. This fast strategy can also be adapted by the three-parameter 3D Radon transform algorithm. Here, the frequency and curvature are combined to create three distinct new parameters, λ_x , λ_y and λ_{xy} . A frequency-independent transform operator can then be constructed. By inverting this operator just once and iteratively reusing the inversion results across all frequency calculations, the algorithm's computational performance is markedly improved. In the paper of Ma (2024) mentioned above, the fast algorithm is also adapted, and the computational efficient λ -f domain three-parameter 3D Radon transform method is proposed.

The amplitude of seismic events varies laterally. Existing 3D Radon transform algorithm only sums the data along a specific path, without considering the events' lateral amplitude variations. This leads to a certain amplitude difference between the multiples separated by the algorithm and the multiples in the original data, affecting the suppression effect. Many scholars have also done related research on improving the amplitude preservation of Radon transform. Nowak and Imhof (2006) and Zhao et al. (2012) analyzed the amplitude preservation of Radon transform and its denoising applications separately. Xue et al. (2012, 2014) and Vyas et al. (2016) proposed the high-order Radon transform algorithms based on different orthogonal polynomials respectively, which added the gradient and curvature information describing the amplitude changes in different directions. They expanded the traditional Radon transform, and made it more accurate in real data processing. Wang et al. (2011) proposed a Radon transform that can simulate the amplitude changes in the seismic data, which also achieved good amplitude preservation results. Tang and Mao

(2014) gave a high-order high-resolution parabolic amplitude-preserving Radon transform, and applied it to 3D seismic data reconstruction. Ma et al. (2020) proposed a method of multiple attenuation using high-order high-resolution 3D Radon transform, which considered the amplitude variation using orthogonal polynomials, and improved the resolution using lower frequencies constraint. Geng et al. (2022) proposed a high-order sparse 3D Radon transform in the mixed time—frequency domain with L1–2 minimization. Here, orthogonal polynomial operator and the fast three-parameter 3D Radon algorithm are combined, and an amplitude preserving algorithm is developed to improve the accuracy of multiple estimation and further enhance multiple suppression effect.

In this paper, we integrate the three-parameter 3D parabolic Radon transform algorithm with an amplitude preservation operator, combining curvature and frequency parameters to propose an amplitude-preserving, anisotropy-considering, fast 3D parabolic Radon transform algorithm. This algorithm can handle lateral amplitude variations in seismic data and only requires the inversion of a single Radon operator, making it computationally efficient. The effectiveness of the algorithm is verified using both synthetic and real seismic data.

It should be noted that the 3D parabolic Radon transform algorithm is studied in the paper and applied to the CDP gathers after NMO correction. A comparative analysis of related algorithms for parabolic Radon transform is also provided. Although hyperbolic Radon transform algorithm can also suppress multiples, as its mechanism differs from the method in this paper, hence it is not included in the analysis and comparisons.

2. Theory

2.1. Regular two-parameter 3D Radon transform (2P 3D Radon)

The two-parameter 3D parabolic Radon transform involves the summation of seismic data along prescribed standard parabolic surfaces, resulting in the 3D Radon domain data. Consider a seismic data represented by $\mathbf{d}(t,x,y)$, where t denotes time, and x and y represent spatial coordinates. The application of 3D parabolic Radon transform yields data in the Radon domain, denoted as $\mathbf{m}(\tau,q_x,q_y)$. Here, q_x and q_y are the curvature parameters in the inline and crossline directions, separately, while τ represents the transformed time coordinate in the Radon domain. By summing data in the

Radon domain along different paraboloids, seismic data in the time-offset domain can be reconstructed, which is

$$\boldsymbol{d}(t,x,y) = \int \int \boldsymbol{m} \left(\tau = t - q_x x^2 - q_y y^2, q_x, q_y\right) \mathrm{d}q_x \mathrm{d}q_y \tag{1}$$

Eq. (1) can be discretized as follows:

$$\mathbf{d}(t,x,y) = \sum_{i=1}^{nqx} \sum_{k=1}^{nqy} \mathbf{m} \Big(\tau = t - q_{xj}x^2 - q_{yk}y^2, q_{xj}, q_{yk} \Big)$$
 (2)

where, nqx and nqy denote the number of q_x and q_y . By transforming both sides of Eq. (2) to frequency domain, we can get

$$\mathbf{D}(\omega, x, y) = \sum_{j=1}^{nqx} \sum_{k=1}^{nqy} \mathbf{M}\left(\omega, q_{xj}, q_{yk}\right) e^{-i\omega\left(q_{xj}x^2 + q_{yk}y^2\right)}$$

$$= \sum_{i=1}^{nqx} \sum_{k=1}^{nqy} e^{-i\omega q_{xj}x^2} \mathbf{M}\left(\omega, q_{xj}, q_{yk}\right) e^{-i\omega q_{yk}y^2}$$
(3)

where D and M are the seismic and Radon domain data in the frequency domain separately.

Eq. (3) can be expressed in two distinct operator notations as follows:

$$\mathbf{D}_{\text{vec}} = \mathbf{L}_{xy} \mathbf{M}_{\text{vec}} \tag{4}$$

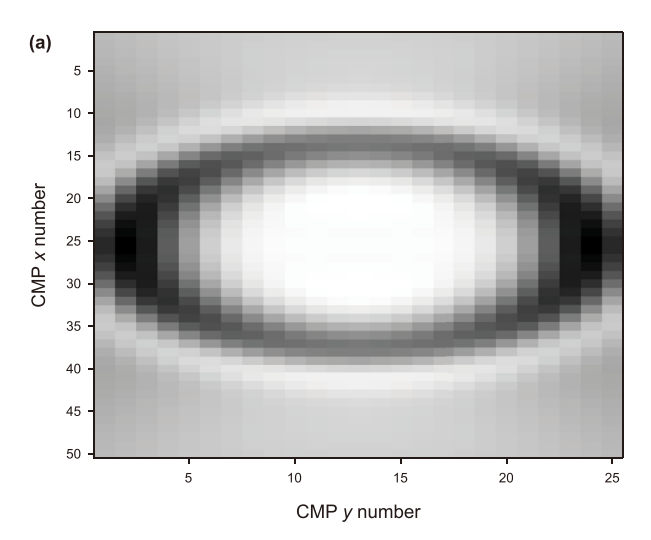
$$\mathbf{D} = \mathbf{L}_{\mathbf{X}} \mathbf{M} \mathbf{L}_{\mathbf{V}} \tag{5}$$

where, \boldsymbol{L}_{x} denotes the matrix associated with the exponential term $\mathrm{e}^{-i\omega q_{yj}x^{2}}$, and \boldsymbol{L}_{y} represents the matrix corresponding to the exponential term $\mathrm{e}^{-i\omega q_{yk}y^{2}}$ in Eq. (3). Furthermore, \boldsymbol{L}_{xy} is a matrix that corresponds to the exponential term of $\mathrm{e}^{-i\omega(q_{xj}x^{2}+q_{yk}y^{2})}$ in Eq. (3). Additionally, $\boldsymbol{D}_{\text{vec}}$ and $\boldsymbol{M}_{\text{vec}}$ are the vectorized forms of the matrixes \boldsymbol{D} and $\boldsymbol{M}_{\text{r}}$ respectively.

For the purpose of balancing computational accuracy and efficiency, the general 3D Radon transform is often resolved utilizing a least-squares algorithm that is related with Eq. (5), which may be expressed as

$$\tilde{\boldsymbol{M}} = \boldsymbol{L}_{x}^{H} \left(\boldsymbol{L}_{x} \boldsymbol{L}_{x}^{H} + \mu \boldsymbol{I} \right)^{-1} \boldsymbol{D} \left(\boldsymbol{L}_{y}^{H} \boldsymbol{L}_{y} + \mu \boldsymbol{I} \right)^{-1} \boldsymbol{L}_{y}^{H}$$
(6)

where, I represents the unit diagonal matrix, μ denotes a damping



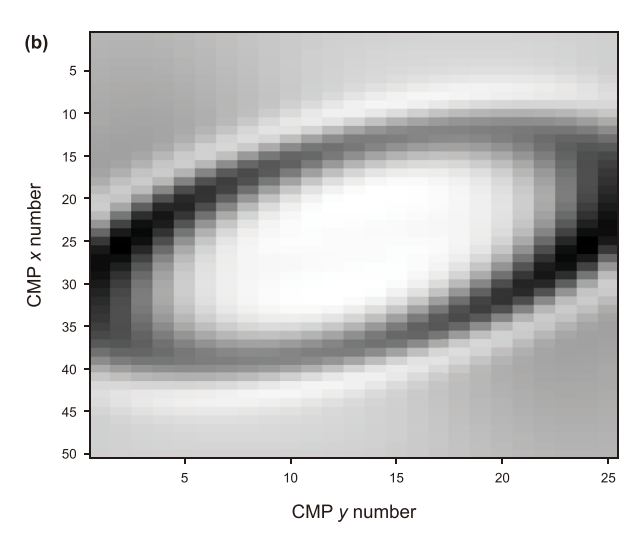


Fig. 1. Time slices of the synthetic data. (a) Upper data slice without anisotropy; (b) lower data slice with anisotropy.

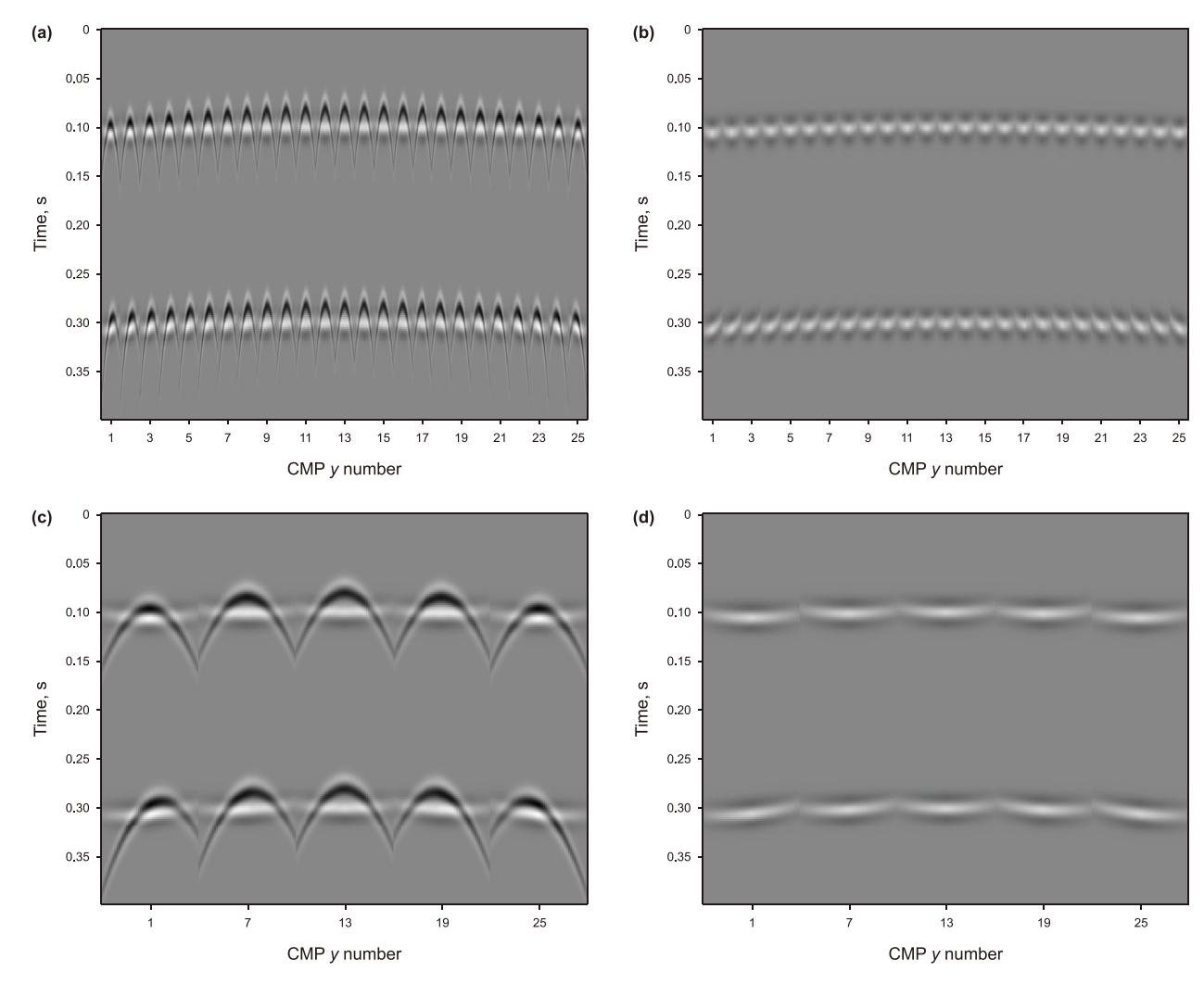


Fig. 2. The small bin gathers of the synthetic data. (a) All bin gathers with multiples; (b) all bin gathers with the true primaries; (c) five small bin gathers with multiples; (d) five small bin gathers with the true primaries.

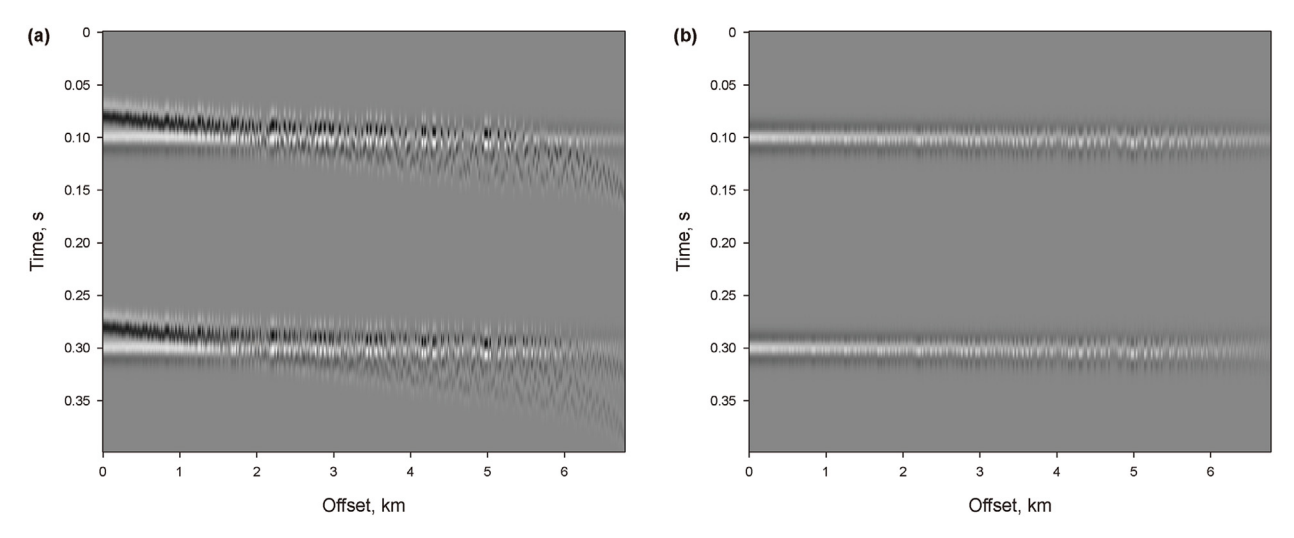


Fig. 3. Sythetic data sorted by scalar offset. (a) Data with multiples; (b) true primaries.

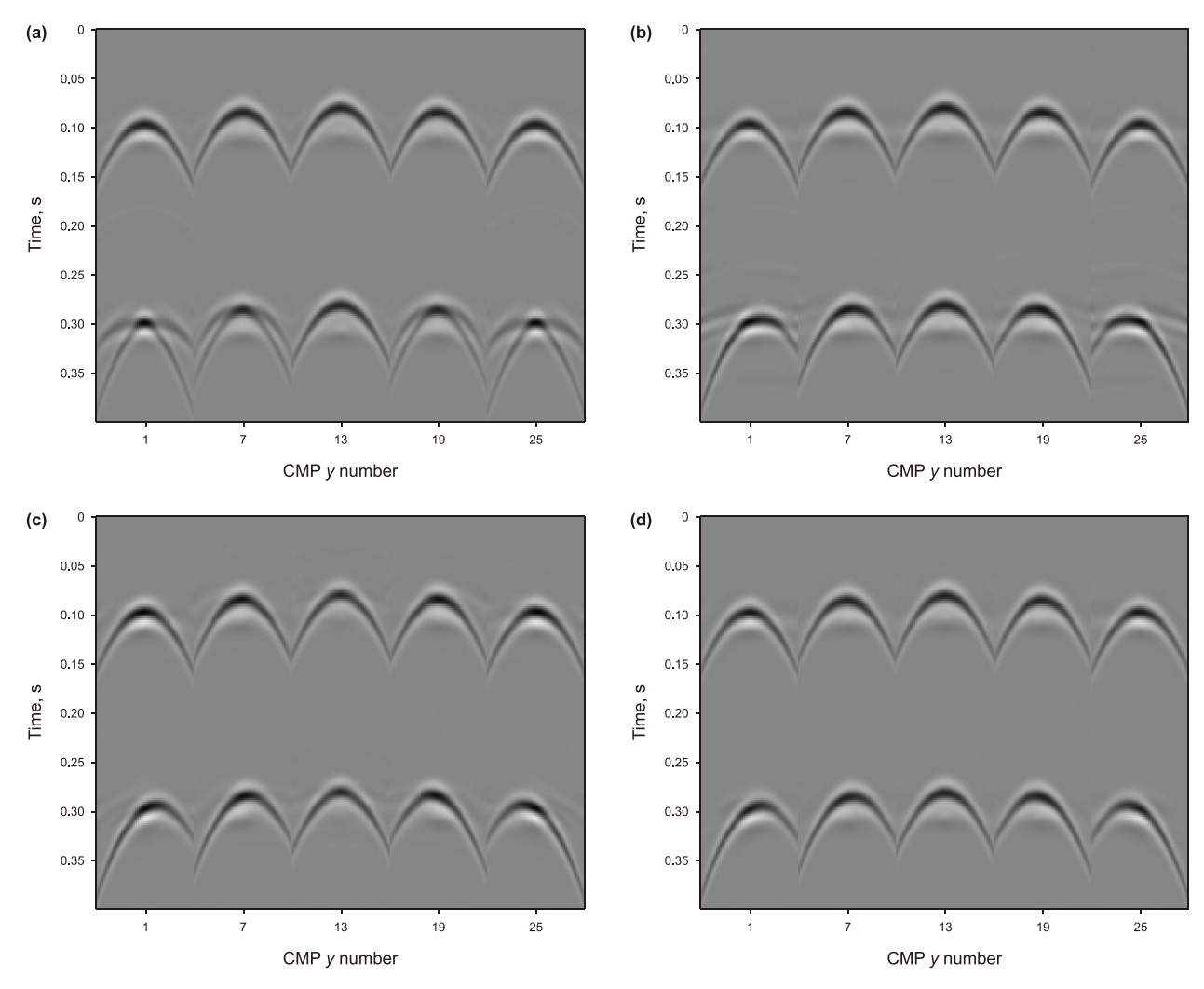


Fig. 4. Multiples estimated by different algorithms. (a) 2P 3D Radon algorithm; (b) HO2P 3D Radon algorithm; (c) 3P 3D Radon algorithm; (d) HO3P 3D Radon algorithm.

factor applied to enhance the stability of the matrix inversion. The damping factor is chosen to lie within the interval (0.01, 1), depending on the specific requirements of the computation. The notation $^{\rm H}$ signifies the conjugate transpose of matrixes under consideration. An alternative solution exists that is related to Eq. (4). However, due to the significantly larger size of the matrix \boldsymbol{L}_{xy} compared to \boldsymbol{L}_x and \boldsymbol{L}_y , the computational expense associated with this method is substantially higher. Consequently, Eqs. (5) and (6) are generally preferred for the implementation of 3D Radon transform.

2.2. Three parameter-3D Radon transform (3P 3D Radon)

Current theoretical approaches posit that in 3D seismic data after normal moveout correction, the time-slice of the multiples conforms to an elliptical shape, with its focal points located on the survey line. This assumption presupposes uniformity in the characteristics of multiples across different azimuths, and a consistent travel-time curve morphology irrespective of direction. The conventional 3D Radon transform employs two curvature parameters along orthogonal survey lines to parameterize the seismic wavefield. In instances where the subsurface geology is simple, this method may suffice; however, in the presence of anisotropy within the earth's strata, the normal moveout corrected multiples' time-slice deviates from the standard elliptical form, with its focal

points displaced from the survey lines. Under such conditions, conventional 3D Radon transform fails to represent the seismic data accurately, potentially leading to incomplete multiple attenuation or primary damage. Therefore, conventional algorithm exhibits inherent limitations when addressing multiple attenuation in seismic data acquired in complex geological structures.

In real data acquisition, the superposition of factors such as cable drifting can significantly enhance the distortion of the timeslice ellipse. To adequately represent the spatially varying seismic wavefield, it becomes necessary to introduce an elliptical rotation parameter. This parameter accounts for the directional variability in seismic data and an adaptive, spatially varied rotated ellipse model is built. Consequently, building on the characteristics of the multiples in 3D seismic data under complex conditions, an additional rotated ellipse parameter q_{xy} is integrated into the 3D Radon transform. This extension leads to a three-parameter (3P) 3D Radon transform, which is employed for the precise representation of seismic data.

In the 3P 3D Radon transform, the elliptical representation of the seismic wave-field is parameterized by the coefficients associated with x^2 , y^2 , and xy, which are denoted as q_x , q_y and q_{xy} , respectively. The introduction of q_{xy} accounts for the rotational aspect of the ellipse, thereby allowing for a more accurate characterization of the seismic data in the presence of complex geological structures and anisotropic media.

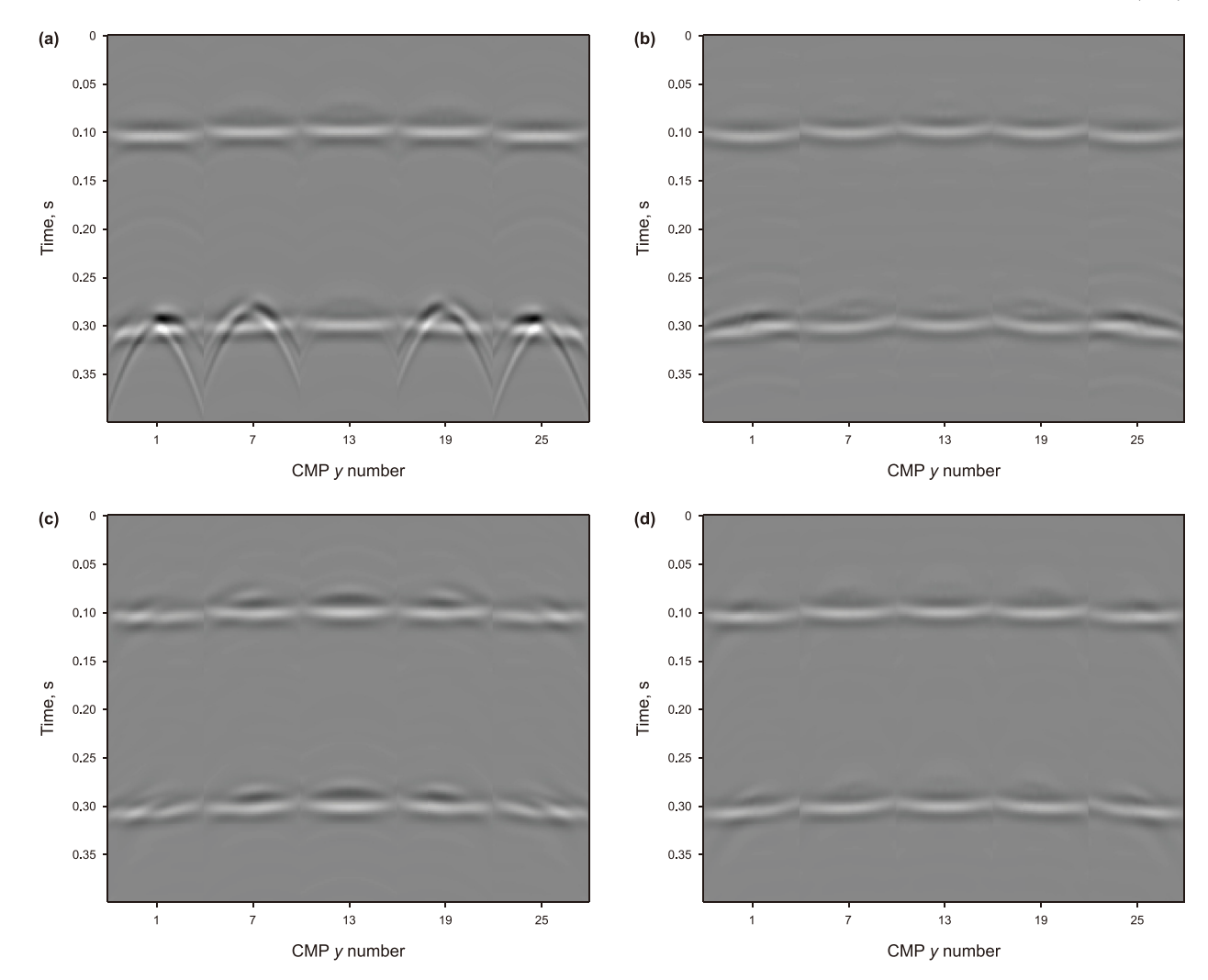


Fig. 5. Multiple suppression results by different algorithms. (a) 2P 3D Radon algorithm; (b) HO2P 3D Radon algorithm; (c) 3P 3D Radon algorithm; (d) HO3P 3D Radon algorithm.

It is well known that the value of q generally represents the residual time of seismic events after normal moveout correction. Specifically, in the case of 3D Radon transform, q_x represents the residual time of parabolic events within small bin gathers after normal moveout correction, while q_y represents the time differences between various small bin gathers across the entire dataset. On the other hand, q_{xy} represents the time difference at both ends of the seismic events within each small bin gather. If a time difference δt exists between the two ends of the small bin gather, then $q_{xy} = \delta t/2$. Additionally, q_{xy} also signifies the rotation of the data's time slices, where $q_{xy} < 0$ indicates a clockwise rotation of the ellipse in the time slice, and $q_{xy} > 0$ indicates a counterclockwise rotation.

The mathematical formulation of the 3P 3D Radon transform can be written as

$$\mathbf{d}(t,x,y) = \iiint \mathbf{m} \left(\tau = t - q_x x^2 - q_y y^2 - q_{xy} xy, q_x, q_y, q_{xy} \right) dq_x dq_y dq_{xy}$$

$$(7)$$

The corresponding discrete form in the frequency domain is

$$\boldsymbol{D}(\omega, x, y) = \sum_{j=1}^{nqx} \sum_{k=1}^{nqy} \sum_{l=1}^{nqxy} \boldsymbol{M}\left(\omega, q_{xj}, q_{yk}, q_{xyl}\right) e^{-i\omega\left(q_{xj}x^2 + q_{yk}y^2 + q_{xyl}xy\right)}$$
(8)

The exponential term in Eq. (8) can be denoted as L_{qxy} . This term comprises five variables, and does not lend itself to be decomposed into small matrix multiplications similar with Eq. (5). Consequently, Eq. (8) can only be expressed in its operator form as follows:

$$\mathbf{D}_{\text{vec}} = \mathbf{L}_{\text{qxy}} \mathbf{M}_{\text{vec}} \tag{9}$$

The corresponding least squares solution is

$$\tilde{\boldsymbol{M}}_{\text{vec}} = \boldsymbol{L}_{qxy}^{\text{H}} \left(\boldsymbol{L}_{qxy} \boldsymbol{L}_{qxy}^{\text{H}} + \mu \boldsymbol{I} \right)^{-1} \boldsymbol{D}_{\text{vec}}$$
(10)

In this formulation, the length of $\tilde{\mathbf{M}}_{\text{vec}}$ is $nqx \cdot nqy \cdot nqxy$, while the length of \mathbf{D}_{vec} is $nx \cdot ny$. The dimension of the matrix \mathbf{L}_{qxy} is $(nx \cdot ny) \times (nqx \cdot nqy \cdot nqxy)$. The matrix \mathbf{L}_{qxy} is considerably large, and the matrix specific to each frequency varies. The computation of the 3P 3D Radon transform necessitates the calculation of matrix inversion for each individual frequency, rendering the algorithm computationally intensive.

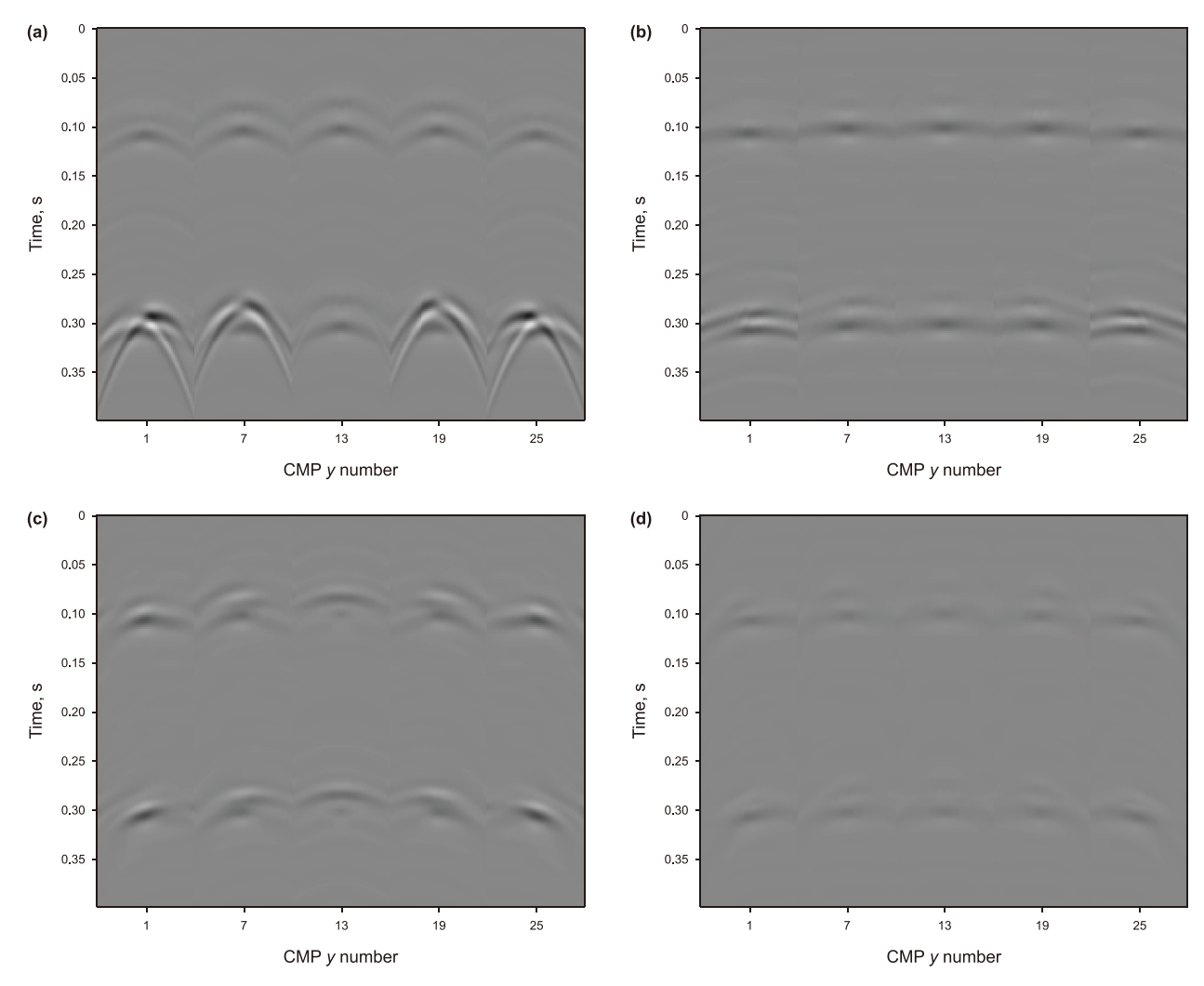


Fig. 6. Difference between suppression results from different algorithms and the true primaries. (a) 2P 3D Radon algorithm; (b) HO2P 3D Radon algorithm; (c) 3P 3D Radon algorithm; (d) HO3P 3D Radon algorithm.

2.3. Fast Radon transforms

In comparison to the 2P 3D Radon transform, the 3P version of the algorithm incorporates an additional parameter, which results in an extra dimension for the transformed data. The 2P algorithm operator can be decomposed into separate operators in the inline and crossline directions, allowing for individual matrix multiplication and inversion operations that reduce computational costs. Conversely, the 3P algorithm's operator accounts for the curvature parameters in both the inline and crossline directions as well as the spatial variations of the elliptical model, which precludes decomposition into distinct operators. The extra dimension leads to significantly more time-consuming multiplication and inversion processes. While the algorithm enables a more precise description of the seismic wavefield, its computational demands are substantial, impeding its widespread industrial application.

To enhance computational efficiency, a new variable $\lambda=qf$ is introduced, which effectively removes the operator's frequency dependency. This modification ensures that all frequencies correspond to a single transform operator, necessitating the calculation of the operator and its inversion only once, with the results being applicable to the processes of all frequencies. By integrating frequency and curvature into one parameter, the algorithm can be

reformulated as a single-operator linear problem, significantly boosting computational efficiency. Generally speaking, the value of λ is calculated by multiplying q with the maximum frequency presented in the data. The Nyquist frequency is not suggested to use here, as it will bring huge computation cost.

With the introduction of the new variable λ , such that $\lambda_x = q_x f$, $\lambda_y = q_y f$ and $\lambda_{xy} = q_{xy} f$, the 3P 3D Radon inverse transform can be reformulated accordingly:

$$\mathbf{D}(f, x, y) = \sum_{j=1}^{nqx} \sum_{k=1}^{nqx} \sum_{l=1}^{nqxy} \mathbf{M}(f, \lambda_{xj}, \lambda_{yk}, \lambda_{xyl}) e^{-2\pi i (\lambda_{xj}x^2 + \lambda_{yk}y^2 + \lambda_{xyl}xy)}$$
(11)

The exponential term in Eq. (11) is designated as the transform operator $L_{\lambda qxy}$, which exhibits independence from frequency. Consequently, the transform operator remains invariant across all frequencies. The operator and its inversion are calculated only once, and then they are called throughout the iteration process. This approach substantially enhances the computational efficiency of the 3P 3D Radon transform.



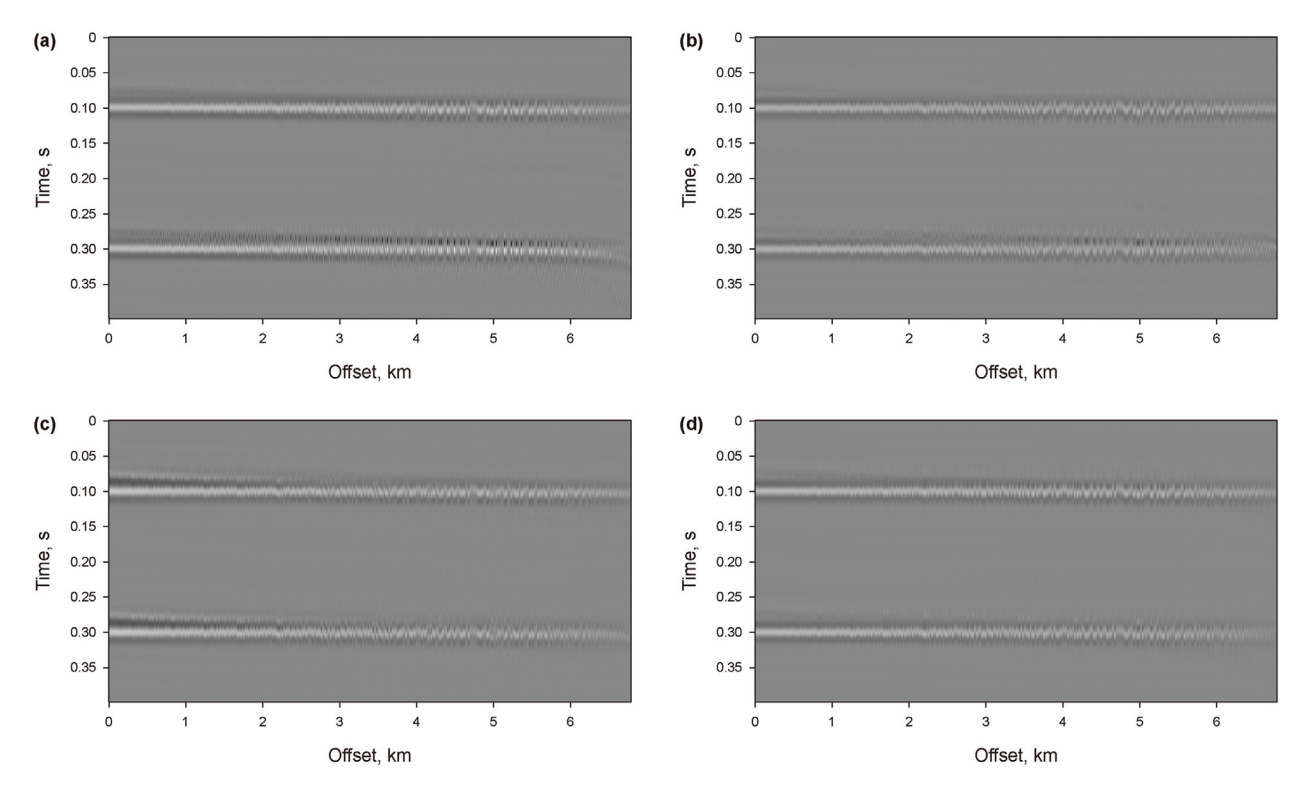


Fig. 7. Multiple suppression results by different algorithms sorted by scalar offset. (a) 2P 3D Radon algorithm; (b) HO2P 3D Radon algorithm; (c) 3P 3D Radon algorithm; (d) HO3P 3D Radon algorithm.

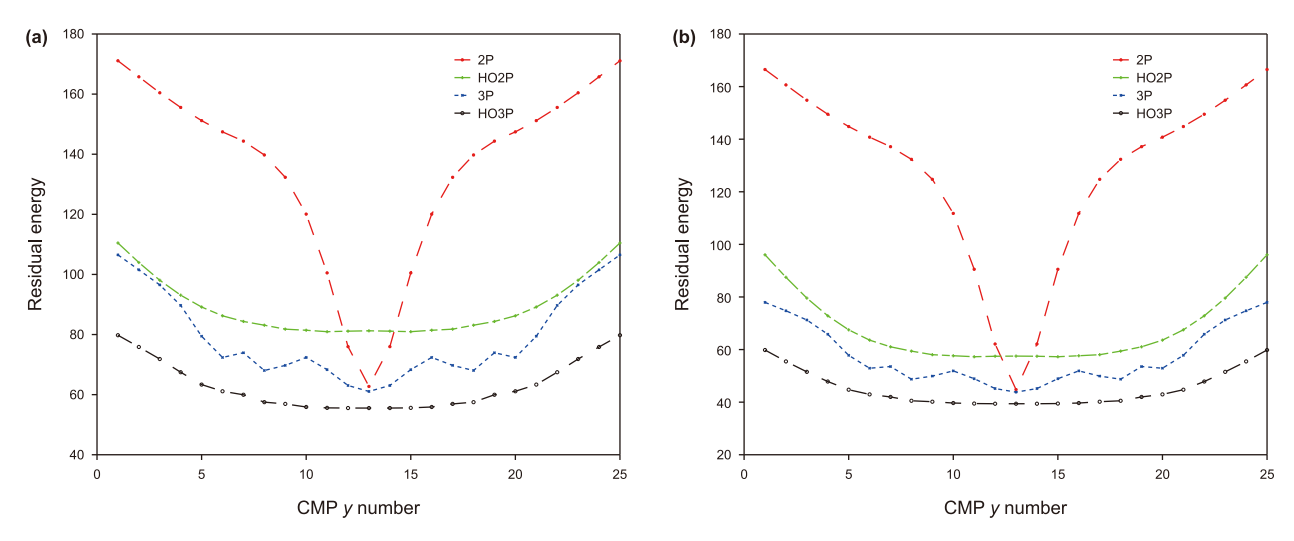


Fig. 8. Residual energy comparison of the four algorithms. (a) Total residual energy; (b) residual energy of the lower part.

Table 1Comparison of computation time used by different algorithms.

Method	2P 3D	HO2P 3D	3P 3D	HO3P 3D
Time, s	0.034	0.328	16.946	160.119

2.4. Amplitude preserving high-order three-parameter 3D Radon transform (HO3P 3D Fast Radon)

The Radon transform algorithm only sums seismic data along a specific path, assuming a constant amplitude in the horizontal direction. However, seismic data amplitude changes with wave-field

propagation, which will reduce transform resolution and cause amplitude losses. Improved methods are needed to address these challenges.

Since the amplitude of seismic data in CDP gathers varies gently, Johansen et al. (1995) used orthogonal polynomials to fit the AVO effect of the data. Xue et al. (2014) combined Radon transform with orthogonal polynomial fitting to propose an amplitude-preserving high-order Radon transform algorithm. In this paper, two orthogonal polynomial coefficients p(x) and p(y) are used to fit the amplitude changes of the seismic data in the x and y directions, respectively, and they are fused into the 3P 3D Radon transform operator.

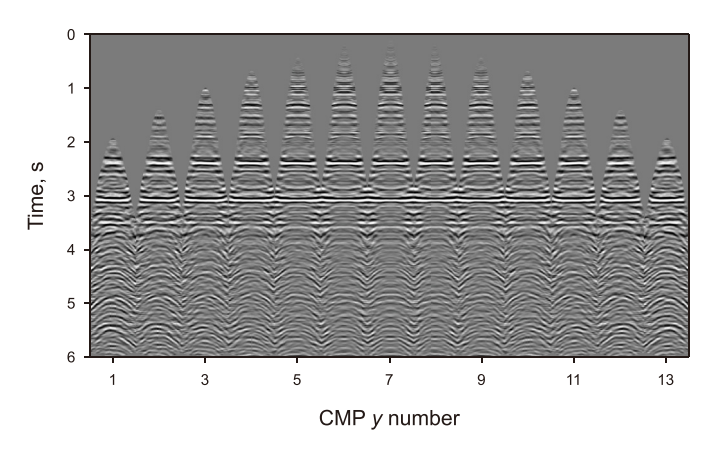
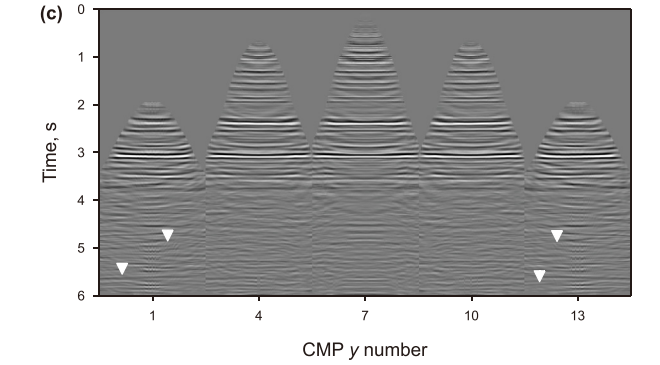


Fig. 9. The small bin gathers of real data.

Take the orthogonal polynomial p(x) in the x direction for example. Let the order of orthogonal polynomial coefficients be 3, then the amplitude preserving operator can be obtained from the following formulas:

$$p_i(x) = \left\{ x^i - \sum_{k=0}^{i-1} \alpha_{ik} p_k(x) \right\} / \alpha_{ii}$$
(12)

$$\alpha_{ii} = \sqrt{\sum_{k=0}^{N} x_k^{2i} - \sum_{k=0}^{i-1} \alpha_{ik}^2}$$
 (13)



$$\alpha_{ik} = \sum_{j=0}^{N} x_j^i p_k(x_j), \quad \alpha_{00} = \sqrt{N}, \quad p_0 = 1 / \alpha_{00}$$
 (14)

where x is the offset, $p_i(x)$ is the polynomial coefficient. $p_1(x)$ represents the summation information, $p_2(x)$ the gradient information, and $p_3(x)$ the curvature information of the amplitude. Similarly, the amplitude preserving operator p(y) corresponding to q_y can be calculated by offset y.

The amplitude-preserving operation can be completed by combining the amplitude-preserving operator with the Radon transform operator, which is

$$\mathbf{D}(f, x, y) = \sum_{j=1}^{nqx} \sum_{k=1}^{nqy} \sum_{l=1}^{nqxy} \mathbf{M}(f, \lambda_{xj}, \lambda_{yk}, \lambda_{xyl})$$

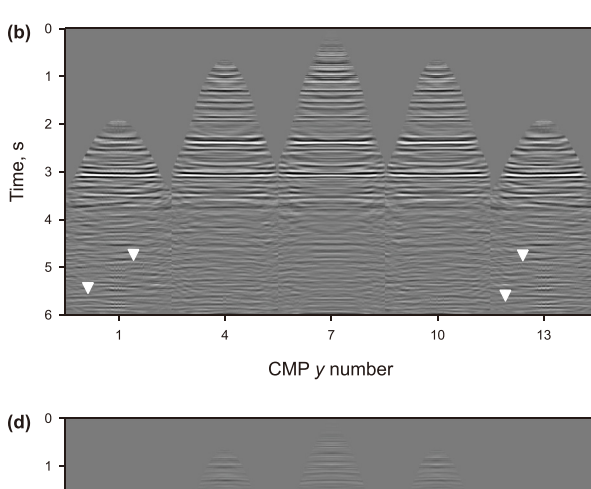
$$p(x)e^{-i2\pi\lambda_{xj}x^2} p(y)e^{-i2\pi\lambda_{yk}y^2} e^{-i2\pi\lambda_{xyl}xy}$$
(15)

3. Examples

To demonstrate the effectiveness of the method proposed in this paper, both simulated and real data are used to test the method.

3.1. Synthetic data examples

We first demonstrate the application of the algorithm on synthetic data. This data consists of 1250 traces, with 50 traces in the *x*-direction at an interval of 195 m, and 25 traces in the *y*-direction at an interval of 400 m. The upper portion of this synthetic data is isotropic, which means that the event shapes across each bin gather are identical, with the maximum multiple residuals in the upper section being up to 60 ms. The lower section of the data is anisotropic, with varying event shapes across the bin gathers, yet the



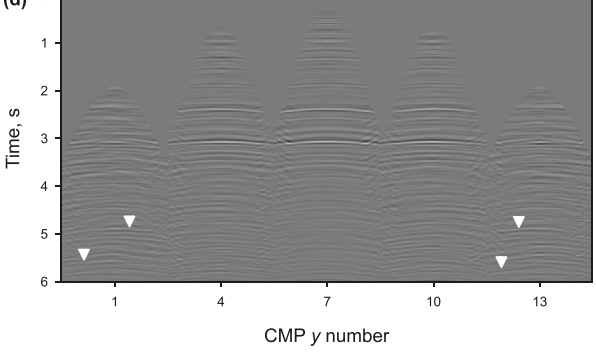


Fig. 10. Real data of selected small bin gathers. (a) Original data, (b) demul result of 3P 3D Radon; (c) demul result of HO3P 3D Radon; (d) difference of (b) and (c).

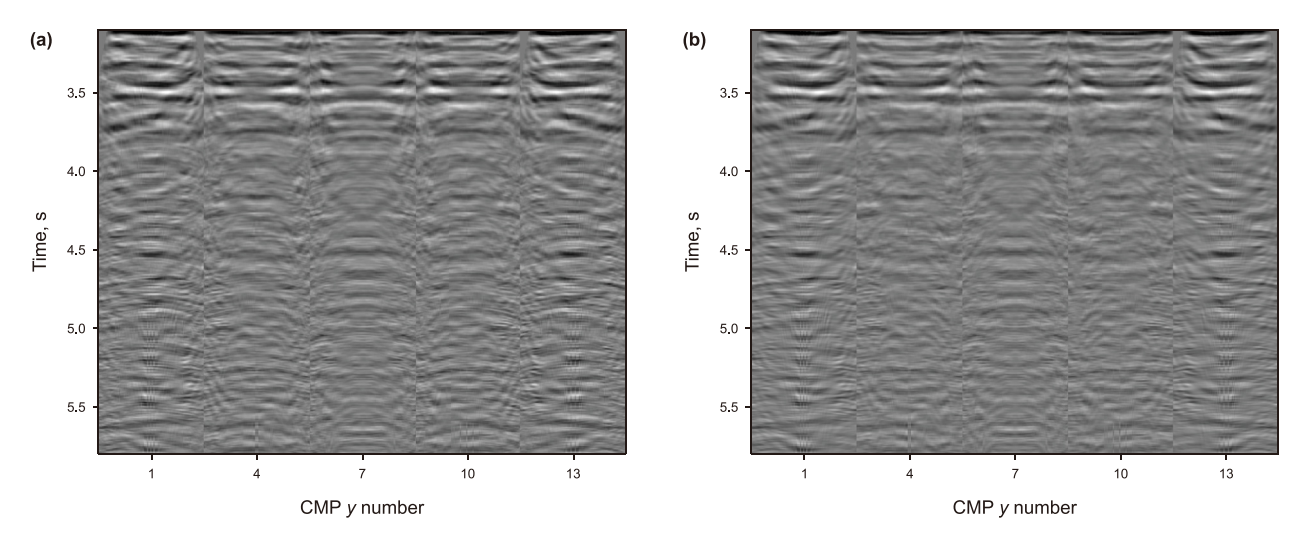


Fig. 11. Partial zoomed section of the demul results in bin gathers. (a) Demul result of 3P 3D Radon; (b) demul result of HO3P 3D Radon.

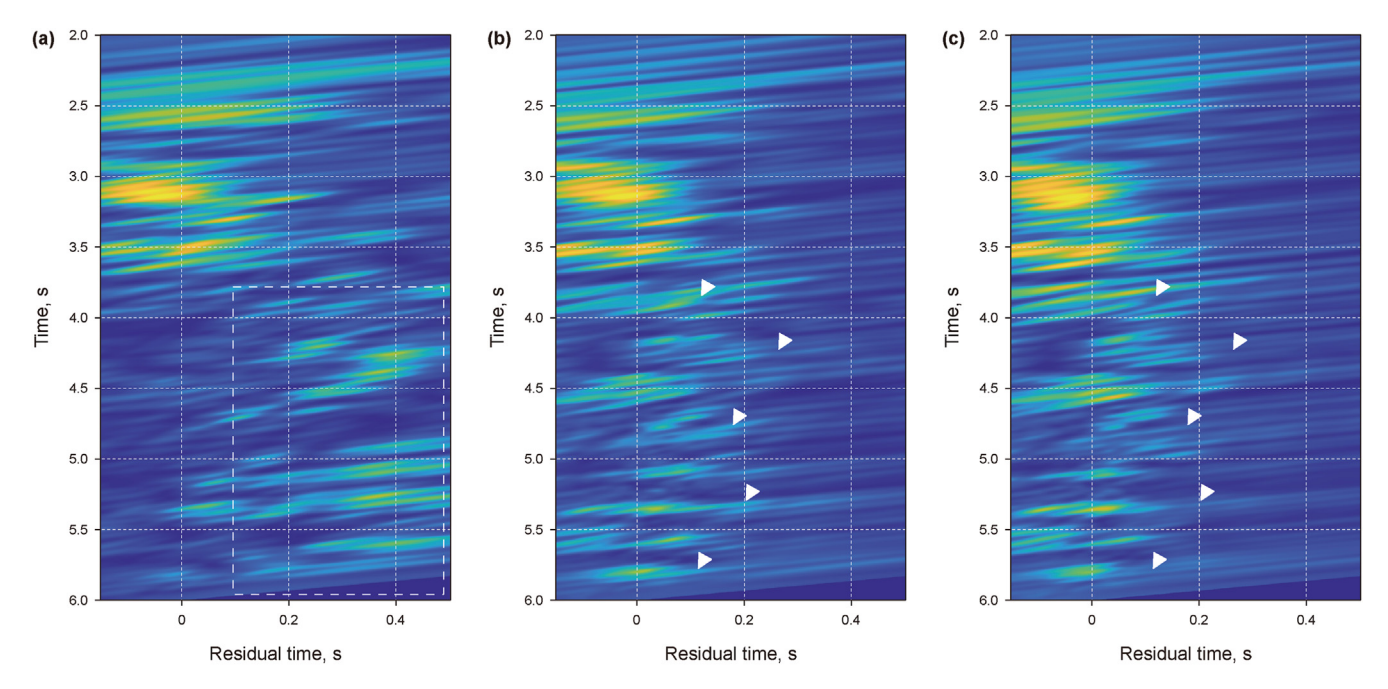


Fig. 12. Radon spectrum of the small bin gather. (a) Original data; (b) demul result of 3P 3D Radon; (c) demul Result of HO3P 3D Radon.

maximum multiple residuals remain at 60 ms. The data exhibits AVO effects horizontally, showing a gradual decrease in amplitude from the center towards both ends. Since the fast Radon transform algorithm outperforms the conventional Radon algorithm (as referenced in Ma (2024)), all results presented in this paper are derived from the computations using the fast algorithms.

Fig. 1 shows the time slices of the data's upper section without anisotropy and the lower section with anisotropy, respectively. It is evident that the upper section, which lacks anisotropy, has a time slice that forms a standard ellipse, whereas the lower section, due to the presence of anisotropy, has a time slice that appears as a rotated ellipse. Within the elliptical trajectory, there are variations in amplitude, with some being stronger and others weaker.

Figs. 2 and 3 illustrate the synthetic data used for testing in this paper. Fig. 2 gives all the bin gathers that include multiples (a) as well as the true primaries (b). To facilitate a better comparison of the suppression results, five small bin gathers are also presented (c,

d). Fig. 3 shows the data containing multiples sorted by scalar offset (a), along with the common cell gathers of the true primaries (b).

In the processing of synthetic data examples, for the sake of fairness, all algorithms adopted the same damping parameters and cut-off parameters. The values of nqx and nqy are set slightly larger than the number of seismic traces in the x and y directions (nxr and nyr), which are 52 and 30 separately, while the value of nqxy is set to 9.

Figs. 4—6 show the results of small bin gathers processed using 2P, high-order two-parameter (HO2P), 3P, and HO3P 3D Radon algorithms, respectively. All algorithms are implemented by the fast single operator method. Fig. 4 displays the multiples estimated by each algorithm, Fig. 5 shows the results after multiple suppression, and Fig. 6 illustrates the difference between the suppression results and the true primaries. From the results, it can be observed that the effectiveness of multiple suppression gradually improves.

The 2P algorithm does not account for the data's azimuthal

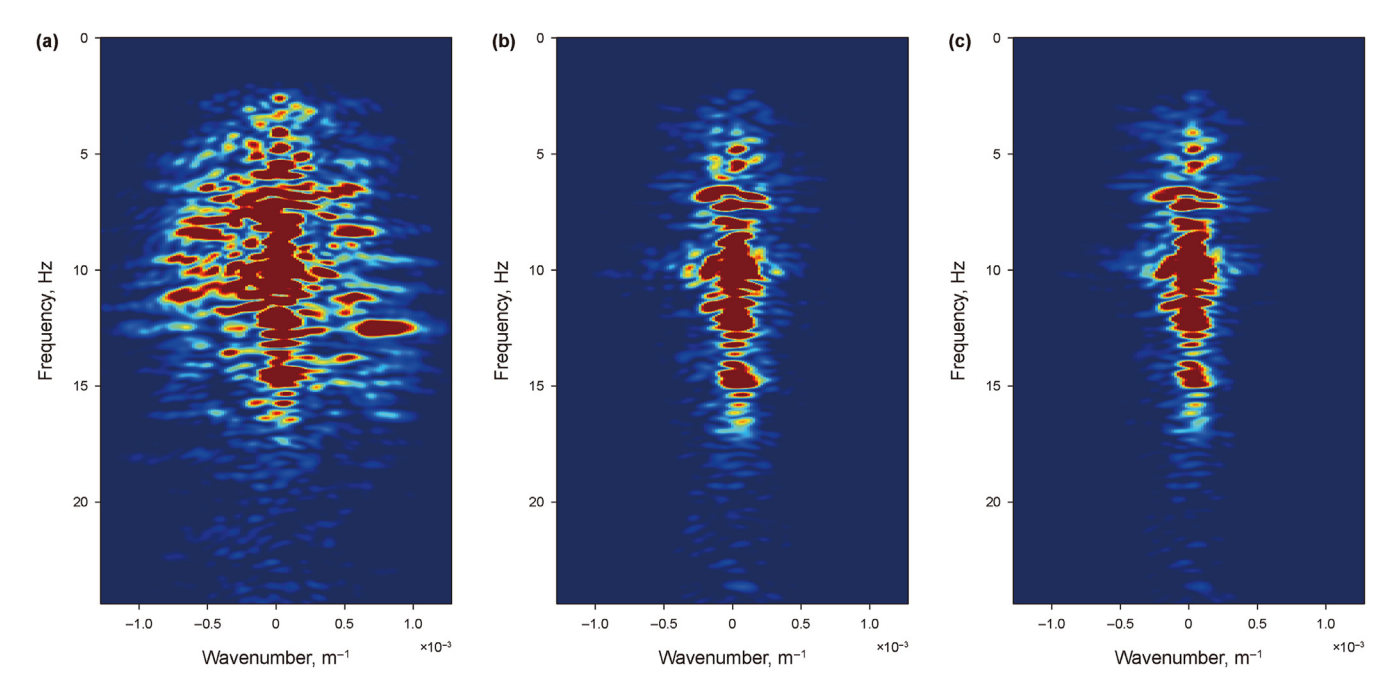


Fig. 13. FK spectrum of the small bin gather. (a) Original data; (b) demul result of 3P 3D Radon; (c) demul result of HO3P 3D Radon.

variation nor does it consider the amplitude's lateral variation. As a result, in Fig. 4(a), the estimated multiples have upper parts whose amplitudes do not match those of the real data multiples, and the lower parts, except for the very center of the small bin gather, show significant differences from the true multiples. This leads to multiple residuals in both the upper and lower parts of the suppression results shown in Fig. 5(a), with severe residuals in the lower part. Fig. 6(a) also reflects the algorithm's shortcomings in amplitude preservation and its failure to consider the azimuthal variation of data.

The HO2P algorithm enhances the 2P algorithm by adding an amplitude preservation operator, which greatly improves the effect of multiple suppression. The amplitude preservation operator can deal with the azimuthal variation of data to a certain extent. Therefore, in Fig. 4(b), the lower part of the estimated multiples essentially matches the original data's morphology. However, due to inherent theoretical limitations of the algorithm, it is not fully capable of addressing the azimuthal variation of data. Consequently, there are still multiple residuals in the suppression results shown in Fig. 5(b). The residuals can also be observed in Fig. 6(b).

The 3P algorithm is a further development of the 2P algorithm, taking into account the azimuthal variation of data. Therefore, the estimated multiples in Fig. 4(c) are completely consistent with the multiples in the data. However, this algorithm does not consider the lateral variation in amplitude, leading to certain differences between the estimated and the true multiples. This results in multiple residuals in the suppression results shown in Fig. 5(c). Yet, as seen from the difference profile in Fig. 6(c), the difference between the suppression results and the true primaries has significantly decreased compared to the previous two algorithms.

The HO3P algorithm comprehensively considers the data's azimuthal variation and the amplitude lateral variation, resulting in the most accurate estimation of multiples (Fig. 4(d)) and the most thorough suppression results (Figs. 5(d) and 6(d)).

Fig. 7 also presents the common cell gathers sorted by scalar offset. It is clear from the gathers that there is progressive improvement in the suppression effects. It should be noted that due to the larger multiple residuals mostly located at near offsets

(Fig. 6(c)), the 3P algorithm has more residuals in the common cell gather at near offsets in Fig. 7(c). However, in terms of overall residual energy, this algorithm has significantly small energy compared to the 2P and HO2P algorithms.

Fig. 8 presents the residual energy curves of different small bin gathers in the multiple suppression results obtained by various algorithms. In Fig. 8(a), the curve values represent the total residual energy of a small bin gather, while the values in Fig. 8(b) are the residual energies of the lower anisotropy data within a small bin gather. Since the residual energy mainly comes from the anisotropic parts at the lower part of the data, the trends of the two curves are consistent. From the figures, it can be seen that the HO3P algorithm has the lowest residual energy, demonstrating its reliability and effectiveness. The 2P algorithm generally has the highest residual energy, but since there is no anisotropy in the middle bin gather, the precision described by this method is the same as that of the 3P algorithm. As anisotropy becomes more severe towards the sides of the data, the 2P algorithm becomes less reliable in describing the data, leading to a sharp increase in residual energy. The HO2P algorithm considers the changes in seismic data amplitude and can cope with data anisotropy to some extent, thus significantly reducing its residual energy compared to the 2P algorithm. The 3P algorithm inherently accounts for the anisotropy of seismic data, so its residual energy is further reduced compared to the HO2P algorithm. However, due to its lack of consideration for lateral variations in amplitude, it still has some residuals. On the other hand, the HO3P algorithm takes into account both the anisotropy of seismic data and the lateral variation of amplitude, resulting in the lowest residual energy.

Table 1 also presents the computation time of the fast algorithms used in this paper. Generally speaking, the calculation time of fast algorithms is only about 5% of that of conventional algorithms. In this case, we will not make a comparison with the calculation time of conventional algorithms. It can be observed from Table 1 that the computation time of the amplitude-preserving algorithm is almost 10 times that of the conventional algorithm. Since all algorithms only perform one matrix multiplication and inversion on the operator matrix, the difference in

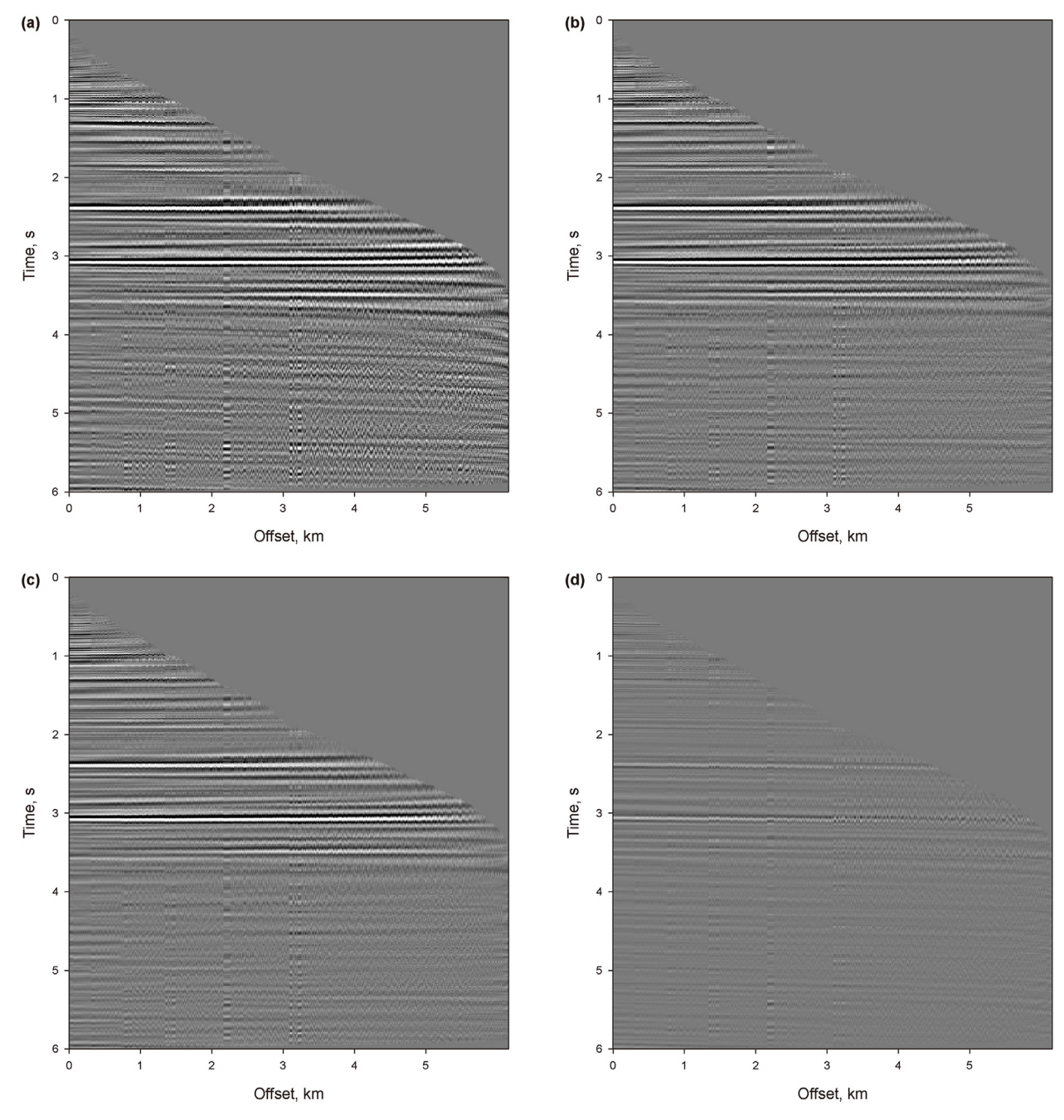


Fig. 14. Real data sorted by scalar offset. (a) Original data, (b) demul result of 3P 3D Radon; (c) demul result of HO3P 3D Radon; (d) difference of (b) and (c).

computational efficiency is mainly due to the operator matrix. In the fast algorithm, the number of variables λ is the same as the number of variables q in the conventional algorithm. For example, the 2P 3D algorithm operates on two small matrices L_x and L_y obtained from the decomposition of a large matrix, with sizes [nxr, nqx] and [nqy, nyr], respectively; the HO2P 3D algorithm also operates on two small matrices obtained from the decomposition of a large matrix, but since it includes an amplitude-preserving operator, the matrix sizes increase, with sizes now being $[nxr, 3 \cdot nqx]$ and $[3 \cdot nqy, nyr]$, respectively. The 3P 3D algorithm cannot decompose the large matrix and must operate on it directly, with the matrix size being $[nxr \cdot nyr, nqx \cdot nqy \cdot nqxy]$, while the HO3P 3D, as an amplitude-preserving algorithm, has a matrix size of $[nxr \cdot nyr, 3 \cdot nqx \cdot 3 \cdot nqy \cdot nqxy]$. The two 3P algorithms have the same inverse

matrix size, both being $[nxr \cdot nyr, nxr \cdot nyr]$, but the HO3P algorithm has a larger amount of matrix multiplication operations, leading to its longer computation time.

Consideration could be given to utilizing the advantages of GPUs in large matrix operations to accelerate the algorithms. Our tests indicate that if 3P algorithms are computed using a GPU, the computation time can be reduced from about 17 s to less than 3 s, significantly improving computational efficiency.

3.2. Real data examples

We further validated the algorithm using real data. Ma et al. (2020) and Ma (2024) also tested the data using a HO2P 3D high-resolution Radon transform and a 3P 3D Radon transform,

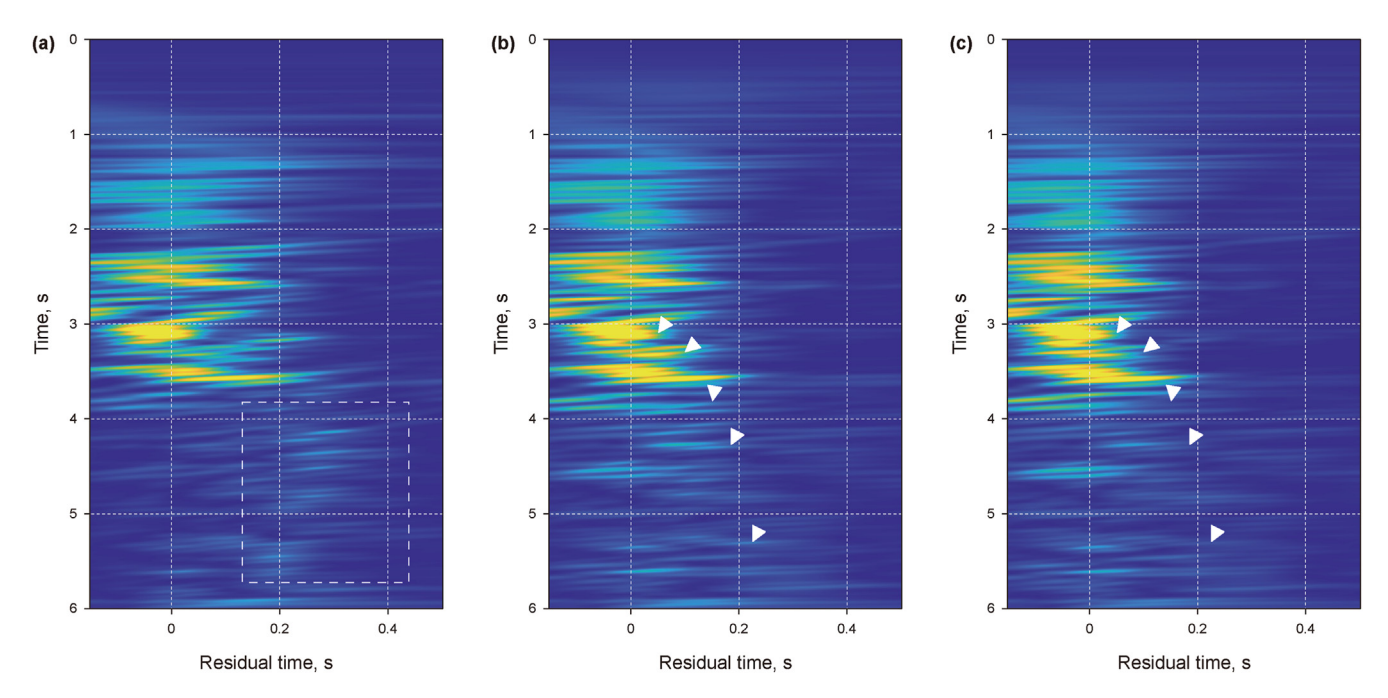


Fig. 15. Radon spectrum of the common cell gather sorted by scalar offset. (a) Original data; (b) demul result of 3P 3D Radon; (c) demul Result of HO3P 3D Radon.

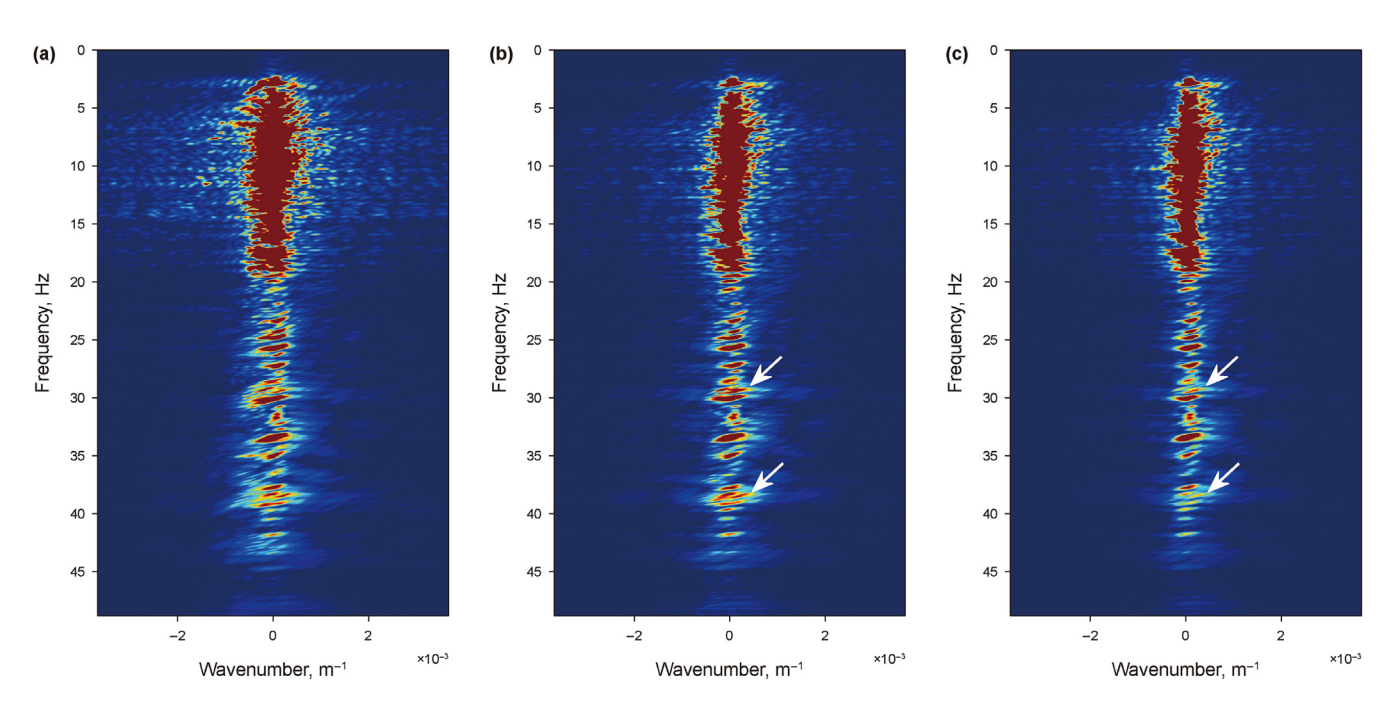


Fig. 16. FK spectrum of the common cell gather sorted by scalar offset. (a) Original data; (b) demul result of 3P 3D Radon; (c) demul result of HO3P 3D Radon.

respectively. Their corresponding processing results can be referred to in the relevant articles. In this test, we only used the 3P 3D fast Radon and the HO3P 3D Fast Radon algorithms for processing and comparative analysis. In the processing of real data, for the sake of fairness, all algorithms adopted the same damping and cut-off parameters.

Fig. 9 shows the small bin gathers of real data. We selected five small bin gathers at equal intervals for a more effective demonstration. Fig. 10 presents the five selected small bin gathers, where Fig. 10(a) shows the original data, Fig. 10(b) displays the results processed by the 3P 3D Radon transform, Fig. 10(c) illustrates the

results after processing with our proposed HO3P algorithm, and Fig. 10(d) shows the difference between the results of Fig. 10(b) and (c). The arrows in all four figures are at the same location, demonstrating that the HO3P algorithm, due to its better amplitude preservation, further suppresses the multiples with horizontal amplitude variations that the 3P algorithm could not suppress. Fig. 11 is a local enlargement from 3 to 5.8 s in Fig. 10(b) and (c), from which it can be seen that the lower part of Fig. 11(b) is cleaner, while Fig. 11(a) has obvious multiple residuals. Figs. 12 and 13 further provide the Radon and FK spectrums of the first small bin gather. The multiple energy in the rectangular of Fig. 12(a) is

attenuated evidently. Compared with Fig. 12(b)'s 3P 3D Radon algorithm, the Radon spectrum of the HO3P algorithm in Fig. 12(c) further suppresses the multiple energy indicated by the arrow. The FK spectrum of Fig. 13(c) is also significantly better focused than that of Fig. 13(b), indicating more thorough suppression of multiples. All these demonstrate the advantages of the HO3P algorithm.

Fig. 14 also compares the common cell gather sorted by scalar offset from the two algorithms, with Fig. 14(c) showing the results of the HO3P algorithm. Compared to the results of the 3P 3D Radon algorithm in Fig. 14(b), the jitter noise below 3 s is reduced, and the data is cleaner. More thorough multiple suppression in the gathers is beneficial for subsequent inversion and reservoir prediction. Figs. 15 and 16 present the Radon and FK spectrums of the common cell gathers, with the arrows again indicating the same positions. It can also be seen from these results that the HO3P 3D Radon algorithm further suppresses the residual multiples, leading to a more focused Radon and FK spectrums after processing.

4. Conclusions and suggestions

We present an improved three-parameter amplitude-preserving 3D fast Radon transform tailored for multiple suppression in complex geological areas. The fast algorithm integrates curvature and frequency into a single parameter, simplifying the algorithm to a single-operator problem, which significantly improves the effectiveness and efficiency of multiple suppression. Building upon the 3P Radon transform, HO3P algorithm enhances the amplitude preservation by incorporating additional operators that describe lateral amplitude variations within the dataset. The efficacy of this new algorithm has been confirmed through both synthetic and real dataset testing, highlighting its superior performance especially when dealing with complex seismic data. Consequently, we can give the following conclusions and suggestions:

- (1) The novel three-parameter amplitude-preserving 3D Radon transform surpasses conventional methods in maintaining data fidelity, playing an important role in the enhancement of seismic data quality.
- (2) Due to the inclusion of more complex mathematical operations, the algorithm now requires significantly more computing power compared to traditional methods. To reduce this increased demand, it is recommended that the operators be further optimized to eliminate unnecessary computations. Matrix blocking, matrix decomposition, and other techniques can also be used to accelerate the computation of large matrices. At the same time, efficient memory storage strategies should be adopted. When dealing with data with uniform geometries, intermediate results can be cached in memory to avoid repetitive calculations, thus speeding up the processing. Moreover, parallel computing resources should be fully utilized. Additionally, GPUs have obvious advantages over CPUs in large-scale matrix operations. It is considered to implement the above algorithm based on GPU.
- (3) The computational cost of the 3P algorithm is already very large, and if we consider its corresponding high-resolution algorithm, iterating to improve resolution for each frequency is not feasible. In the fast algorithm proposed in this paper, referring to the idea of Chen and Lu (2011), we can consider a non-iterative high-resolution strategy using the results calculated from dominant-frequency to constrain the computations at other frequencies. Since this approach involves the inversion processing of only one frequency, the computational cost does not increase significantly. Moreover,

- we can consider combining the above idea with GPU computing to further improve computational efficiency.
- (4) With proper adjustment, this method can also be used in seismic data reconstruction and denoising.

CRediT authorship contribution statement

Ji-Tao Ma: Writing — review & editing, Writing — original draft, Methodology, Investigation, Data curation, Conceptualization. **Kai-Ge Zhao:** Formal analysis. **Zhen Liao:** Investigation.

Declaration of competing interest

The authors declare that they have no known competing financial interests or personal relationships that could have appeared to influence the work reported in this paper.

Acknowledgement

This work was supported in part by National Natural Science Foundation of China (NSFC) under grant 42274139 and in part by the R&D Department of China National Petroleum Corporation (Investigations on fundamental experiments and advanced theoretical methods in geophysical prospecting applications, 2022DQ0604-03).

References

- Abbad, B., Ursin, B., Porsani, M.J., 2011. A fast, modified parabolic Radon transform. Geophysics 76 (1), V11–V24. https://doi.org/10.1190/1.3532079.
- Beylkin, G., 1987. Discrete radon transform. IEEE Trans. Acoust. Speech Signal Process. 35, 162–172. https://10.1109/TASSP.1987.1165108.
- Cao, W.P., Ross, W.S., 2017. High-resolution 3D tau-p transform by matching pursuit. In: 87th Annual International Meeting. SEG Expanded Abstracts, pp. 4302–4306. https://doi.org/10.1190/segam2017-17741549.1.
- Cary, P.W., 1998. The simplest discrete Radon transform. In: 68th Annual International Meeting, SEG Expanded Abstracts, pp. 1999–2002. https://doi.org/10.1190/1.1820335.
- Chen, Z.H., Lu, W.K., 2011. Non-iterative high resolution radon transform. In: 73rd Annual International Conference and Exhibition Incorporating SPE EUROPEC. EAGE Extended Abstracts. https://doi.org/10.3997/2214-4609.20149534.
- Donati, M.S., Martin, N.W., 1995. Seismic reconstruction using a 3D tau-p transform. CREWES Research Report 7, 111–1116.
- Geng, W.H., Li, J.Y., Chen, X.H., et al., 2022. 3D high-order sparse Radon transform with L1-2 minimization for multiple attenuation. Geophys. Prospect. 70 (4), 655–676. https://doi.org/10.1111/1365-2478.13185.
- Hampson, D., 1986. Inverse velocity stacking for multiple elimination. J. Can. Soc. Explor. Geophys. 22. 44–55.
- Herrmann, P., Mojesky, T., Magesan, M., et al., 2000. De-aliased, high-resolution Radon transforms. In: 70th Annual International Meeting, SEG Expanded Abstracts, pp. 1953–1956. https://doi.org/10.1190/1.1815818.
- Hugonnet, P., Boelle, J.L., Mihoub, M., 2008. High resolution 3D parabolic Radon filtering. In: 78th Annual International Meeting. SEG Expanded Abstracts, pp. 2492–2496. https://doi.org/10.1190/1.3063861.
- Hugonnet, P., Boelle, J.L., Mihoub, M., et al., 2009. 3D High resolution parabolic Radon filtering. In: 71st Annual International Conference and Exhibition Incorporating SPE Europec. EAGE Extended Abstracts. https://doi.org/10.3997/ 2214-4609.201400428.
- Johansen, T.A., Bruland, L., Lutro, J., 1995. Tracking the amplitude versus offset (AVO) by using orthogonal polynomials. Geophys. Prospect. 43 (2), 169–184. https://doi.org/10.1111/j.1365-2478.1995.tb00134.x.
- Li, Z.N., Li, Z.C., Wang, P., et al., 2013. Multiple attenuation using λ-f domain high-resolution Radon transform. Appl. Geophys. 10 (4), 433–441. https://doi.org/10.1007/s11770-013-0405-1
- Li, Z.X., Li, Z.C., 2017. Accelerated parabolic Radon domain 2D adaptive multiple subtraction with fast iterative shrinkage thresholding algorithm and its application in parabolic Radon domain hybrid demultiple method. J. Appl. Geophys. 143, 86–102. https://doi.org/10.1016/j.jappgeo.2017.04.014.
- Lu, W.K., 2013. An accelerated sparse time-invariant Radon transform in the mixed frequency-time domain based on iterative 2D model shrinkage. Geophysics 78 (4), V147–V155. https://doi.org/10.1190/geo2012-0439.1.
- Ma, J.T., 2024. A 3D fast Radon transform algorithm based on deflecting ellipse model and its application on multiple attenuation. Acta Geophys. 72, 177–193. https://doi.org/10.1007/s11600-023-01093-6.
- Ma, J.T., 2022. Multiple attenuation using 3D high precision radon transform

algorithm based on deflecting ellipse model. In: 83rd EAGE Annual Conference & Exhibition, EAGE Extended Abstracts. https://doi.org/10.3997/2214-4609.202210880

- Ma, J.T., Xu, G.Y., Chen, X.H., et al., 2020. Multiple attenuation with 3D high-order high-resolution parabolic Radon transform using lower frequency constraints. Geophysics 85 (3), V317–V320. https://doi.org/10.1190/geo2018-0742.1.
- Nowak, E.J., Imhof, M.G., 2006. Amplitude preservation of Radon-based multiple-removal filters. Geophysics 71 (5), V123–V126. https://doi.org/10.1190/12243711
- Sacchi, M.D., Ulrych, T.J., 1995. High-resolution velocity gathers and offset space reconstruction. Geophysics 60 (4), 1169–1177. https://doi.org/10.1190/1.1443845.
- Stoffa, P.L., Buhl, P., Diebold, J.B., et al., 1981. Direct mapping of seismic data to the domain of intercept time and ray parameter—a plane-wave decomposition. Geophysics 450, 255–267. https://doi.org/10.1190/1.1441197.
- Sun, W.Z., Li, Z.C., Qu, Y.M., 2022. The 3D conical Radon transform for seismic signal processing. Geophysics 87 (5), V481–V504. https://doi.org/10.1190/geo2021-0278.1.
- Sun, W.Z., Li, Z.C., Qu, Y.M., et al., 2019. Multiple attenuation using λ-f domain high-order and high-resolution Radon transform based on SL0 norm. Appl. Geophys. 16 (4), 473–482. https://doi.org/10.1007/s11770-019-0795-9.
- Tang, H.H., Mao, W.J., 2014. Amplitude preserved seismic data reconstruction by 3D high-order parabolic Radon transform. Chin. J. Geophys. 57 (9), 2918–2927. https://doi.org/10.6038/cjg20140917 (in Chinese).
- Thorson, J.R., Claerbout, J.F., 1985. Velocity-stack and slant-stack stochastic inversion. Geophysics 456, 2727–2741. https://doi.org/10.1190/1.1441893.
- Vyas, M., Etgen, J., Liao, Q.Q., 2016. Sparse Radon transform in extended domain. In: 86th Annual International Meeting, SEG Expanded Abstracts, pp. 4540–4544. https://doi.org/10.1190/segam2016-13845990.1.
- Wang, B.F., Zhang, Y.Q., Lu, W.K., et al., 2019. A robust and efficient sparse time-

- invariant radon transform in the mixed time—frequency domain. IEEE Trans. Geosci. Rem. Sens. 57 (10), 7558—7566. https://doi.org/10.1109/TGRS.2019.2914086.
- Wang, B., Sacchi, M.D., Yin, X.Y., 2011. AVO-preserving sparse parabolic Radon transform. In: 73rd EAGE Conference and Exhibition Incorporating SPE EUROPEC 2011. Extended Abstracts. https://doi.org/10.3997/2214-4609.20149215.
- Wang, L.L., Mao, W.J., Tang, H.H., et al., 2017. Amplitude preserved seismic data reconstruction by fast 3D parabolic Radon transform. Chin. J. Geophys. 60 (7), 2801–2812. https://doi.org/10.6038/cjg20170725 (in Chinese).
- Xie, J.F., Wang, X., Wang, X.W., et al., 2021. Multiple-suppression method using the λ-f domain high-resolution parabolic Radon transform with curvature magnification. Appl. Geophys. 18 (2), 1–10. https://doi.org/10.1007/s11770-021-0883-5.
- Xue, Y.R., Ma, J.T., Chen, X.H., 2012. Multiples attenuation based on directional orthogonal polynomial transform. Chin. J. Geophys. 55 (10), 3450–3458. https://doi.org/10.6038/j.issn.0001-5733.2012.10.028 (in Chinese).
- Xue, Y.R., Ma, J.T., Chen, X.H., 2014. High-order sparse Radon transform for AVO-preserving data reconstruction. Geophysics 79 (2), V13–V22. https://doi.org/10.1190/geo2013-0002.1.
- Yilmaz, O.Z., Taner, M.T., 1994. Discrete plane-wave decomposition by least-mean-square-error method. Geophysics 59 (6), 973–982. https://doi.org/10.1190/1.1443657.
- Zhang, Y.Q., Lu, W.K., 2014. 2D and 3D prestack seismic data regularization using an accelerated sparse time-invariant Radon transform. Geophysics 79 (5), V165–V177. https://doi.org/10.1190/geo2013-0286.1.
- Zhao, X., Dong, L.G., Shan, L.Y., 2012. Amplitude preservation theoretical analysis of Radon transforms de-noising method. Oil Geophys. Prospect. 47 (6), 858–867 (in Chinese).